Coherent transfer of optical vortices via backward four-wave mixing in a double-Λ atomic system

Chun Meng, Tao Shui ⬡,[*] and Wen-Xing Yang ⬡[†]

School of Physics and Optoelectronic Engineering, Yangtze University, Jingzhou, Hubei, 434023, China

We propose and analyze an efficient scheme for the coherent transfer of optical vortices in a cold atomic ensemble with four-level double-Λ configuration. The orbital angular-momentum (OAM) information can be transferred from the incident vortex fields to the generated backward signal field via resonant backward four-wave mixing (FWM). Considering the single vortex probe field initially acting on one transition of the atomic ensemble and using experimentally achievable parameters, we identify the conditions under which the resonant backward FWM allows us to greatly improve the conversion efficiency of optical vortices beyond what is achievable in the resonant forward OAM transfers. It is found that the complete energy conversion of optical vortices originates from the perfect competition between linear absorption and parametric gain. We also demonstrate that the phase mismatching would be detrimental to the high-efficiency transfer of optical vortices. Furthermore, we show that the generated backward signal field develops a new pure or mixing OAM state when the control field is also a vortex beam. Finally, we investigate the composite vortex beam generated by collinear superposition of the incident vortex probe and signal fields, which can controlled via adjusting the intensity of the control field. Our scheme may have potential applications in OAM-based optical communication and optical information processing.

I. INTRODUCTION

In the past several decades, the study of optical vortices has been one of the hot spots in the field of optics due to their applications in optical manipulation [1], optical communication [2,3], and optical tweezers [4]. As a new type of laser beam, an optical vortex carrying an orbital angular momentum (OAM) of $l\hbar$ per photon contains a helical phase term $e^{il\phi}$, where ϕ is the azimuthal angle and l is the topological charge (or azimuthal index) [5]. Typical optical vortices such as a Laguerre-Gaussian (LG) beam [6], Bessel-Gauss (BG) beam [7], and perfect vortex beam [8] exhibit a doughnut-shaped intensity pattern with a phase singularity at the central dark spot. In 1992, Allen *et al.* first proposed and experimentally observed the optical vortex beam [9]. Since then, significant efforts have been made to explore the generation and detection of an optical vortex beam [10–14]. Meanwhile, the exchange and manipulation of optical vortices have also been extensively investigated in a variety of structures and materials, such as liquid crystal films [15], metamaterials [16,17], and Dammann vortex gratings [18]. However, these studies are performed without all-optical controllable capabilities.

On the other hand, based on the combination of electromagnetically induced transparency (EIT) [19] and standing waves, the atomic ensemble provides a promising platform for the spatially dependent light-matter interaction. Up to now, a host of breakthroughs have been made such as atom localization [20,21], electromagnetically induced gratings [22,23],

controllable photonic band gaps [24,25], and PT symmetry [26,27]. By using a vortex beam to replace the standing wave, numerous schemes for the spatially dependent light-matter interaction have been proposed and many intriguing quantum optical phenomena have been discovered, such as light-induced torque [28], vortex-induced transparency and absorption [29–31], spatially structured Kerr nonlinearity [32], Rydberg atomic localization [33], storage and retrieval of light beams carrying OAM [34,35], and vortex wave mixing [36–48]. Such proposals have the obvious advantages of all-optical controllable and reconfigurable capabilities.

Among these investigations, the transfer of light beams with OAM is always an important issue due to its potential applications in quantum information process [49,50]. For instance, the OAM is transferred from the strong control field to the weak probe field with the storage and retrieval of light [34,35] and two-component slow light [46]. The helical phase twist of the generated four-wave mixing (FWM) field is coherently engineered (enhanced or suppressed as desired) via the field-detuning modulation in vortex FWM processes [39–42]. Meanwhile, the OAM transfer between the two weak probe fields takes place via the coherent superposition of the ground states [47] and noise-induced coherence [48], in which the limit of 25% transfer efficiency cannot be broken due to the resonant light-matter interaction. Several nonlinear schemes for improving the vortex conversion efficiency have been proposed via utilizing three-wave mixing in the Autler–Townes splitting regime [44] and using the rather complicated spatial modulations of two control fields in the forward FWM process [45]. Accordingly, the transfer efficiency of optical vortices is observed to arrive at 60% and 100%, respectively. Recently, the transfer of optical vortices also has been studied in

---

[*]Corresponding author: ahushuitao@126.com

[†]Corresponding author: wenxingyang2@126.com

solid-state systems, such as quantum wells [51–53], quantum dots [54,55], rare-earth-ion-doped solids [56], molecular magnets [57], and graphene [58].

In this paper, we investigate the coherent transfer of optical vortices in a cold atomic ensemble with a four-level double-Λ configuration. The OAM state can be transferred from the incident vortex fields to the generated signal field via resonant backward FWM process. We demonstrate that the generated signal field has the same vorticity as the incident probe field when only the incident probe field is a vortex beam. Under the condition of the matched control and pump intensities, the complete energy conversion of light beams with OAM can be achieved in a dense atomic medium with a large optical depth (OD), which is greatly improved compared with previous OAM transfer schemes [44,47,48,51,52,54,57]. Different from the mechanism of OAM transfer with the efficiency of 100% in a previous investigation [45], the high-efficiency vortex transfer originates from the perfect competition between linear absorption and parametric gain in backward FWM. It is also shown that phase mismatch would be detrimental to the high-efficiency transfer of optical vortices. Furthermore, we investigate the intensity and helical phase distributions of the generated backward signal field under different OAM combinations of the vortex probe and control fields. It is found that the signal field would develop a new OAM state with auxiliary assist of the vortex control field. Finally, a composite vortex beam generated by collinear superposition of the incident vortex probe and signal fields has been explored and one can effectively manipulate the intensity and helical phase patterns of the composite vortex beam via adjusting the intensity of the control field. Our scheme may have potential applications in OAM-based optical communication and optical information processing.

II. MODEL AND EQUATIONS

As schematically shown in Fig. 1(a), we consider a four-level double-Λ atomic system with two ground states $|1\rangle$ and $|2\rangle$ and two excited states $|3\rangle$ and $|4\rangle$. This atomic system can be realized in cold ^{87}Rb atoms with $|5S_{1/2}, F = 1\rangle$, $|5S_{1/2}, F = 2\rangle$, $|5P_{1/2}, F = 1\rangle$ and $|5P_{1/2}, F = 2\rangle$ acting as states $|1\rangle$, $|2\rangle$, $|3\rangle$, and $|4\rangle$, respectively. In the proposed system, the transitions $|4\rangle \rightarrow |2\rangle$ and $|3\rangle \rightarrow |2\rangle$ are driven by a strong control field Ω_{c1} (central frequency ω_{c1} and wave vector $\vec{k}_{c1}$) and a strong pump field Ω_{c2} (central frequency ω_{c2} and wave vector $\vec{k}_{c2}$), respectively. Simultaneously, a weak probe field Ω_p (central frequency ω_p and wave vector $\vec{k}_p$) and a weak signal field Ω_s (central frequency ω_s and wave
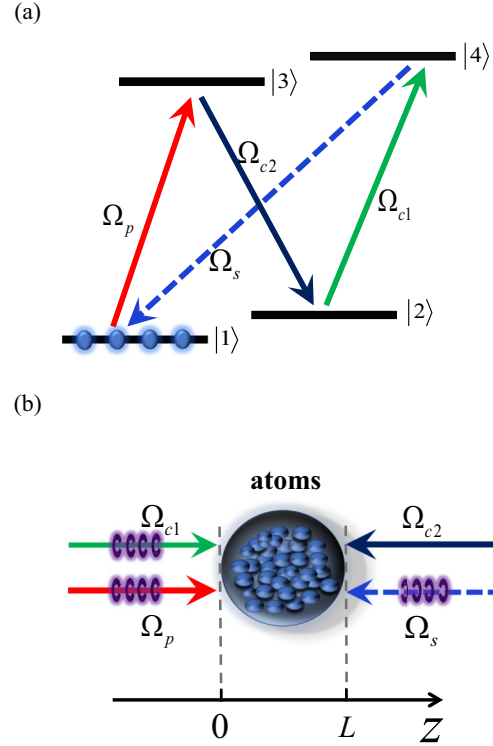

FIG. 1. (a) Schematic diagram of a four-level double-Λ atomic system. (b) Simple block diagram of atomic sample with four optical fields.

vector $\vec{k}_s$) form the wave-mixing process $|1\rangle \rightarrow |3\rangle \rightarrow |2\rangle \rightarrow |4\rangle \rightarrow |1\rangle$. In our proposal, we only consider the condition that the four applied fields are resonant with the corresponding transitions, so that the central frequencies of the applied fields fulfill the relationship $\omega_p - \omega_{c2} + \omega_{c1} = \omega_s$. Therefore, under the electric-dipole and rotating-wave approximations, the interaction Hamiltonian for the four-level double-Λ system can be described by ($\hbar = 1$)

$$H_I = -(\Omega_p|3\rangle\langle1| + \Omega_{c2}|3\rangle\langle2| + \Omega_{c1}|4\rangle\langle2|$$
$$+ \Omega_s|4\rangle\langle1| + \text{H.c.}),\tag{1}$$

where H.c. means Hermitian conjugate. $\Omega_p = \mu_{31}E_p/2\hbar$, $\Omega_{c1} = \mu_{42}E_{c1}/2\hbar$, $\Omega_{c2} = \mu_{32}E_{c2}/2\hbar$, and $\Omega_s = \mu_{41}E_s/2\hbar$ denote the Rabi frequencies of the probe, control, pump, and signal fields with μ_{mn} ($m = 3, 4; n = 1, 2$) being the relevant electric-dipole matrix element.

The equations of motion for density-matrix elements can be obtained as

$$\frac{\partial \rho_{11}}{\partial t} = \Gamma_{31}\rho_{33} + \Gamma_{41}\rho_{44} + i\Omega_p^*\rho_{31} + i\Omega_s^*\rho_{41} - i\Omega_p\rho_{13} - i\Omega_s\rho_{14},\tag{2}$$

$$\frac{\partial \rho_{22}}{\partial t} = \Gamma_{32}\rho_{33} + \Gamma_{42}\rho_{44} + i\Omega_{c2}^*\rho_{32} + i\Omega_{c1}^*\rho_{42} - i\Omega_{c2}\rho_{23} - i\Omega_{c1}\rho_{24},\tag{3}$$

$$\frac{\partial \rho_{33}}{\partial t} = -(\Gamma_{31} + \Gamma_{32})\rho_{33} + i\Omega_p\rho_{13} + i\Omega_{c2}\rho_{23} - i\Omega_p^*\rho_{31} - i\Omega_{c2}^*\rho_{32},\tag{4}$$

$$\frac{\partial \rho_{21}}{\partial t} = -\gamma_{21}\rho_{21} + i\Omega_{c2}^*\rho_{31} + i\Omega_{c1}^*\rho_{41} - i\Omega_p\rho_{23} - i\Omega_s\rho_{24},\tag{5}$$

$$\frac{\partial \rho_{31}}{\partial t} = -\gamma_{31}\rho_{31} + i\Omega_p(\rho_{11} - \rho_{33}) + i\Omega_{c2}\rho_{21} - i\Omega_s\rho_{34}, \tag{6}$$

$$\frac{\partial \rho_{41}}{\partial t} = -\gamma_{41}\rho_{41} + i\Omega_s(\rho_{11} - \rho_{44}) + i\Omega_{c1}\rho_{21} - i\Omega_p\rho_{43}, \tag{7}$$

$$\frac{\partial \rho_{32}}{\partial t} = -\gamma_{32}\rho_{32} + i\Omega_{c2}(\rho_{22} - \rho_{33}) + i\Omega_p\rho_{12} - i\Omega_{c1}\rho_{34}, \tag{8}$$

$$\frac{\partial \rho_{42}}{\partial t} = -\gamma_{42}\rho_{42} + i\Omega_{c1}(\rho_{22} - \rho_{44}) + i\Omega_s\rho_{12} - i\Omega_{c2}\rho_{43}, \tag{9}$$

$$\frac{\partial \rho_{43}}{\partial t} = -\gamma_{43}\rho_{43} + i\Omega_s\rho_{13} + i\Omega_{c1}\rho_{23} - i\Omega_p^*\rho_{41} - i\Omega_{c2}^*\rho_{42}, \tag{10}$$

with $\rho_{11} + \rho_{22} + \rho_{33} + \rho_{44} = 1$ and $\rho_{ij} = \rho_{ji}^*$. Γ_{ij} ($i = 3, 4; j = 1, 2$) is the spontaneous-emission decay rate from level $|i\rangle$ to level $|j\rangle$. The decay rate γ_{mn} of the coherence in transition $|m\rangle \rightarrow |n\rangle$ is defined as $\gamma_{mn} = (\Gamma_m + \Gamma_n)/2$, where $\Gamma_4 = \Gamma_{42} + \Gamma_{41}$ and $\Gamma_3 = \Gamma_{32} + \Gamma_{31}$. Considering D1 line in the cold ^{87}Rb atoms, $\Gamma_3/2 = \Gamma_4/2 = \gamma = \pi \times 5.75$ MHz and $\Gamma_{41} = \Gamma_{42} = \Gamma_{31} = \Gamma_{32} = \gamma$ [59]. For simplicity, we assume $\gamma_{41} = \gamma_{42} = \gamma_{31} = \gamma_{32} = \gamma_{43}/2 = \gamma$ and $\gamma_{21} = 0$.

For the selected atomic system, we assume that both the probe and signal fields are much weaker than the control and pump fields, i.e., $\Omega_p, \Omega_s \ll \Omega_{c1}, \Omega_{c2}$, and the atoms are initially in the ground state $|1\rangle$. As a result, the depletion of the ground state $|1\rangle$ can be neglected [46] and all atoms remain in the ground state $|1\rangle$, i.e., $\rho_{11} = 1$, $\rho_{22} = \rho_{33} = \rho_{44} = 0$. Then, the steady-state analytical solutions of ρ_{31} and ρ_{41} can be obtained as

$$\rho_{31} = \frac{i|\Omega_{c1}|^2\Omega_p}{\gamma(|\Omega_{c2}|^2 + |\Omega_{c1}|^2)} - \frac{i\Omega_{c2}\Omega_{c1}^*\Omega_s}{\gamma(|\Omega_{c2}|^2 + |\Omega_{c1}|^2)}, \tag{11}$$

$$\rho_{41} = \frac{i|\Omega_{c2}|^2\Omega_s}{\gamma(|\Omega_{c2}|^2 + |\Omega_{c1}|^2)} - \frac{i\Omega_{c2}^*\Omega_{c1}\Omega_p}{\gamma(|\Omega_{c2}|^2 + |\Omega_{c1}|^2)}. \tag{12}$$

As shown in Fig. 1(b), we consider a resonant backward FWM process in a cold ^{87}Rb atomic medium with the geometrical length of L. In this arrangement, both the control field Ω_{c1} and the probe field Ω_p propagates through the atomic ensemble in the forward $(+z)$ direction, while the pump field Ω_{c2} propagates through the atomic medium in the backward $(-z)$ direction. Limited by the phase-match condition, the generated signal field Ω_s propagates along the $-z$ axis. Under the slowly varying envelope approximation, the Maxwell's equations, which describe the propagation of the forward probe field Ω_p and the backward signal field Ω_s, can be expressed as

$$\frac{\partial \Omega_p}{\partial z} + \frac{1}{c}\frac{\partial \Omega_p}{\partial t} = i\frac{1}{2k_p}\nabla_\perp^2 \Omega_p + i\frac{\alpha_p\gamma}{2L}\rho_{31}, \tag{13}$$

$$-\frac{\partial \Omega_s}{\partial z} + \frac{1}{c}\frac{\partial \Omega_s}{\partial t} = i\frac{1}{2k_s}\nabla_\perp^2 \Omega_s + i\frac{\alpha_s\gamma}{2L}\rho_{41}, \tag{14}$$

where $\alpha_p = N\sigma_{13}L$ ($\alpha_s = N\sigma_{14}L$) is the OD of the probe (signal) transition. N is the atomic density, and σ_{13} (σ_{14}) is the atomic absorption cross section of the probe (signal) transition. Note that the OD can be effectively controlled by adjusting the atomic density N or geometrical length L. The minus signal of the space-derivative term in Eq. (14) indicates that the propagation direction of the signal field is opposite that of the probe field in the backward FWM process. It should be noted that the diffraction terms containing the transverse

derivatives $\nabla_\perp^2 \Omega_p$ and $\nabla_\perp^2 \Omega_s$ can be safely neglected when the Rayleigh ranges of the probe and signal fields are much larger than the geometrical length of the atomic ensemble, i.e., $\pi w^2/\lambda \gg L$ [45,46]. In this work, the geometrical length of the atomic medium is chosen as $L = 14$ mm [60] and the characteristic transverse size of the probe and signal beams is $w = 0.5$ mm. The wavelengths of the probe and signal fields are $\lambda_p \approx \lambda_s \approx 795$ nm. Then we can obtain $\pi w^2/\lambda_{p(s)} \approx 987$ mm $\gg 14$ mm. Thus, the diffraction terms in Eqs. (13) and (14) can be safely neglected in the following.

Our interest is in the atomic response to the long probe and signal pulses, such that $(1/c)\partial\Omega_{p(s)}/\partial t = 0$. In this situation, the Maxwell's equations (13) and (14) are simplified to

$$\frac{\partial \Omega_p}{\partial z} = i\frac{\alpha_p\gamma}{2L}\rho_{31}, \tag{15}$$

$$-\frac{\partial \Omega_s}{\partial z} = i\frac{\alpha_s\gamma}{2L}\rho_{41}, \tag{16}$$

Substituting Eqs. (11) and (12) into Eqs. (15) and (16) and assuming $\alpha_p = \alpha_s = \alpha$, $\Omega_p(z = 0) = \Omega_p(0)$ and $\Omega_s(z = L) = 0$, we can obtain the expressions of the probe and signal fields at the position z inside the atomic medium as

$$\Omega_p(z) = \frac{|\Omega_{c2}|^2 - e^{(\frac{z}{L}-1)s}|\Omega_{c1}|^2}{|\Omega_{c2}|^2 - e^{-s}|\Omega_{c1}|^2}\Omega_p(0), \tag{17}$$

$$\Omega_s(z) = \frac{1 - e^{(\frac{z}{L}-1)s}}{|\Omega_{c2}|^2 - e^{-s}|\Omega_{c1}|^2}\Omega_{c2}^*\Omega_{c1}\Omega_p(0), \tag{18}$$

with

$$s = \frac{\alpha(|\Omega_{c2}|^2 - |\Omega_{c1}|^2)}{2(|\Omega_{c2}|^2 + |\Omega_{c1}|^2)}, \tag{19}$$

for $|\Omega_{c1}| \neq |\Omega_{c2}|$. Under the condition of $|\Omega_{c1}| = |\Omega_{c2}|$, the expressions of the probe and signal fields can be written as

$$\Omega_p(z) = \frac{\alpha(1 - z/L) + 4}{\alpha + 4}\Omega_p(0), \tag{20}$$

$$\Omega_s(z) = \frac{\alpha(1 - z/L)}{\alpha + 4}\Omega_p(0). \tag{21}$$

III. RESULTS AND DISCUSSIONS

Before presenting the numerical results, the spatial profiles of the vortex beams should be given. We assume that the waist position of the vortex beam is also localized at the plane $z = 0$ in Fig. 1(b). For the selected parameters of the system, the Rayleigh ranges of the probe and signal fields are much larger than the geometrical length of the atomic ensemble,
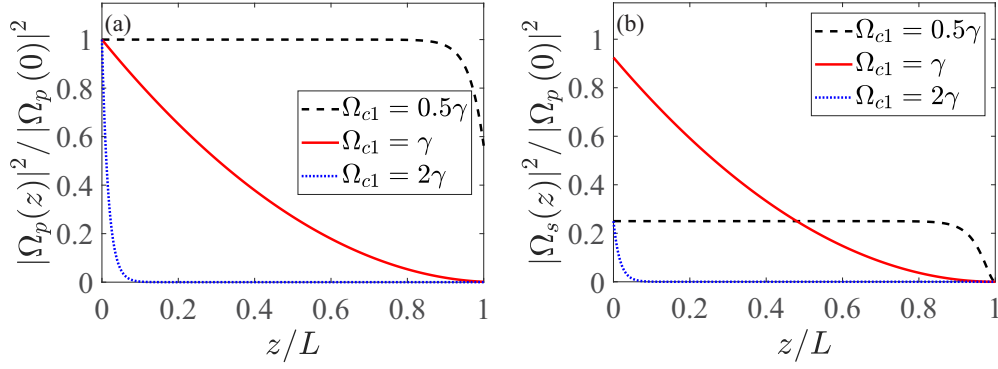
FIG. 2. The dimensionless intensities of (a) the probe field $|\Omega_p(z)|^2/|\Omega_p(0)|^2$ and (b) the signal field $|\Omega_s(z)|^2/|\Omega_p(0)|^2$ versus the dimensionless distance z/L for different intensities of the control field Ω_{c1}. Other parameters are $\Omega_{c2} = \gamma$, $\Omega_{p_0} = 0.01\gamma$, and $\alpha = 100$.

i.e., $\pi w^2/\lambda_{p(s)} \gg L$. In this situation, the vortex beam can be treated as a collimated beam, i.e., the transverse field distribution is almost unchanged, when propagating inside the cold atomic ensemble. Therefore, a unique OAM mode can be given by Laguerre-Gaussian (LG) mode and its Rabi frequency can be expressed cylindrically as [6,54]

$$\Omega_i(r, \phi) = \Omega_{i_0} \frac{1}{\sqrt{|l|!}} \left(\frac{\sqrt{2}r}{w} \right)^{|l|} L_p^{|l|} \left(\frac{2r^2}{w^2} \right) e^{-r^2/w^2} e^{il\phi}, \quad (22)$$

where Ω_{i_0}, w, l, and p represent the intensity, beam waist, topological charge (TC), and radial index (RI) of the LG_p^l mode, respectively. Here, the associated Laguerre polynomial $L_p^{|l|}$ can be expressed as

$$L_p^{|l|}(x) = \frac{e^x x^{-|l|}}{p!} \frac{d^p}{dx^p} (x^{|l|+p} e^{-x}), \quad (23)$$

with $x = 2r^2/w$ determining the radial dependence of the LG beam. In the case of $l \neq 0$, the LG light beam possess OAM along the optical axis.

A. Transfer of optical vortices

In this section, the focus is on investigating the coherent transfer of optical vortices via resonant backward FWM process. Equations (18) and (21) imply that the Rabi frequency of the generated backward signal field is proportional to the Rabi frequencies of the forward probe and control fields. Thus, the signal field Ω_s is a vortex beam if any of the fields Ω_p, Ω_{c1}, or both of them are vortex beams. In the following, we study the coherent transfer of optical vortices for two cases: (a) only the probe field Ω_p is a vortex beam; (b) both the probe field Ω_p and the control field Ω_{c1} are vortex beams.

1. First case: Only Ω_p is a vortex beam

In this case, only the incident probe field at $z = 0$ is a LG mode, which can be expressed by Eq. (22). According to Eqs. (18) and (21), the backward signal field $\Omega_s(z)$ is generated with the same vorticity as the incident probe field $\Omega_p(0)$. In the following, we focus on the conversion efficiency of optical vortices in the backward FWM process.

We first investigate the influence of the control field Ω_{c1} on the transfer of optical vortices. Figures 2(a) and 2(b) show the

evolution of the dimensionless intensities $|\Omega_p(z)|^2/|\Omega_p(0)|^2$ and $|\Omega_s(z)|^2/|\Omega_p(0)|^2$ with the dimensionless distance z/L inside the atomic ensemble for different intensities of the control field. As shown in Figs. 2(a), the forward vortex probe field significantly decreases when passing through the cold atomic medium. Accordingly, part of the energy of the incident probe field is transferred to the generated backward signal field via backward FWM [see Fig. 2(b)]. More importantly, the nonlinear vortex conversion between the probe and signal fields takes place in different spatial regions of the atomic ensemble for different values of Ω_{c1}. Specifically, the vortex transfer mainly takes place at $0.9L \leqslant z \leqslant L$ for $\Omega_{c1} = 0.5\gamma$ [see the black dashed lines in Figs. 2(a) and 2(b)] and $0 \leqslant z \leqslant 0.1L$ for $\Omega_{c1} = 2\gamma$ [see the blue dotted lines in Figs. 2(a) and 2(b)]. In either case, the vortex conversion efficiency at the outport port (i.e., $z = 0$) of the backward signal field, which is governed by $\eta = |\Omega_s(0)|^2/|\Omega_p(0)|^2$, only arrives at 25%. In the case of $\Omega_{c1} = \gamma$, the backward FWM takes place in the whole region (i.e., $0 \leqslant z \leqslant L$) of the atomic medium and the conversion efficiency of optical vortices reaches its maximal value of 92% [see the red solid lines in Figs. 2(a) and 2(b)]. Therefore, the matched control and pump Rabi frequencies (i.e., $|\Omega_{c1}| = |\Omega_{c2}|$) are the optimal condition for achieving the high-efficiency transfer of optical vortices.

Then we consider the optimal condition and explore the dependence of the conversion of optical vortices on the OD of the atomic ensemble. We plot the variation in space of the dimensionless intensities $|\Omega_p(z)|^2/|\Omega_p(0)|^2$ and $|\Omega_s(z)|^2/|\Omega_p(0)|^2$ for different ODs in Figs. 3(a) and 3(b), respectively. One can find that the forward probe field monotonically decreases as z increases from 0 to L, while the backward signal field monotonically increases as z decreases from L to 0. More importantly, the increase of the OD would decrease the intensity of the output probe field at $z = L$ and increase the intensity of the output signal field at $z = 0$. For a dilute atomic medium with a small OD of 5, the conversion efficiency of optical vortices is only 30.9% [see the black dashed lines in Figs. 3(a) and 3(b)]. As the OD increases to 10, the conversion efficiency can be improved to 51% [see the red solid lines in Figs. 3(a) and 3(b)]. In contrast, for a dense atomic medium with a large OD of 500, almost all probe energy is transferred to the generated signal field with the high conversion efficiency of 98.4% [see the blue dotted
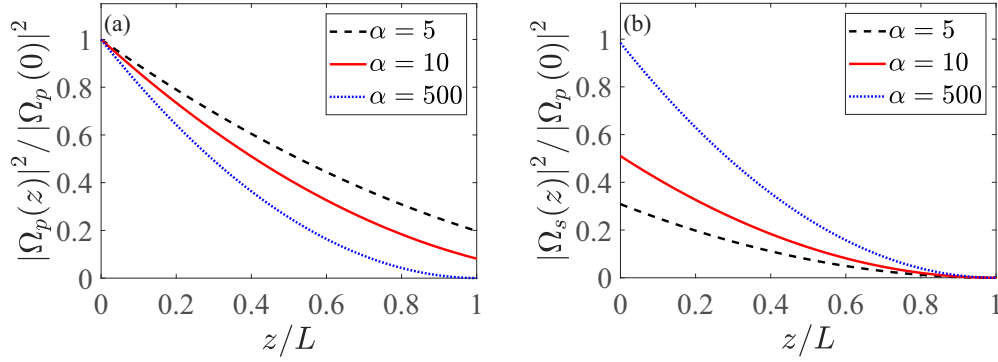
FIG. 3. The dimensionless intensities of (a) the probe field $|\Omega_p(z)|^2/|\Omega_p(0)|^2$ and (b) the signal field $|\Omega_s(z)|^2/|\Omega_p(0)|^2$ versus the dimensionless distance z/L for different ODs α. $\Omega_{c1} = \gamma$ and other parameters are the same as in Fig. 2.

lines in Figs. 3(a) and 3(b)]. In experiment, it is feasible to push the OD of a cold atomic cloud up to the 1000 level [60]. Thus, a complete energy conversion between light beams carrying OAM can be achieved via the resonant backward FWM process. These results offer us another control parameter to improve the conversion efficiency of optical vortices in resonant backward FWM process.

The above interesting feature of transfer of optical vortices originates from the competition of linear absorption and parametric gain [61,62]. Note that the first terms on the right sides of Eqs. (11) and (12) represent the linear absorption of the probe and signal fields, respectively, while the second terms denote the parametric gain. For a small OD of 5, $\Omega_p(z) > \Omega_s(z)$ is always satisfied inside the atomic medium [see the black dashed lines in Figs. 3(a) and 3(b)]. In this case, the unbalance condition [i.e., $\Omega_{c1}\Omega_p(z) > \Omega_{c2}\Omega_s(z)$] gives rise to an imperfect competition between the probe (signal) absorption and parametric gain, thereby leading to the nonzero ρ_{31} and ρ_{41}. Accordingly, the existence of the spontaneous emission from excited states $|3\rangle$ and $|4\rangle$ limits the conversion efficiency of optical vortices. For a large OD of 500, $\Omega_p(z) \approx \Omega_s(z)$

[see the blue dotted lines in Figs. 3(a) and 3(b)]. The detailed balance condition [i.e., $\Omega_{c1}\Omega_p(z) = \Omega_{c2}\Omega_s(z)$] is nearly satisfied inside the atomic medium, which results in a perfect competition between the linear absorption and parametric gain (i.e., $\rho_{31} = \rho_{41} = 0$). Hence, the backward FWM automatically suppresses the spontaneous emission in the whole dense atomic medium, and thereby greatly improving the vortex conversion efficiency.

To give a direct insight into the transfer of optical vortices, we derive the expression of the output signal field at $z = 0$ as

$$\Omega_s(z=0) = \frac{(1-e^{-s})\Omega_{c2}^*\Omega_{c1}}{|\Omega_{c2}|^2 - e^{-s}|\Omega_{c1}|^2}\Omega_p(0) \qquad (24)$$

for $|\Omega_{c1}| \neq |\Omega_{c2}|$, and

$$\Omega_s(z=0) = \frac{\alpha}{\alpha+4}\Omega_p(0) \qquad (25)$$

for $|\Omega_{c1}| = |\Omega_{c2}|$. We plot the intensity and phase patterns of the output signal field at $z = 0$ for different LG modes of the incident probe field in Fig. 4. We take $\Omega_{p_0} = 0.01\gamma$, $\alpha = 500$, and the other parameters are the same as in Fig. 3.
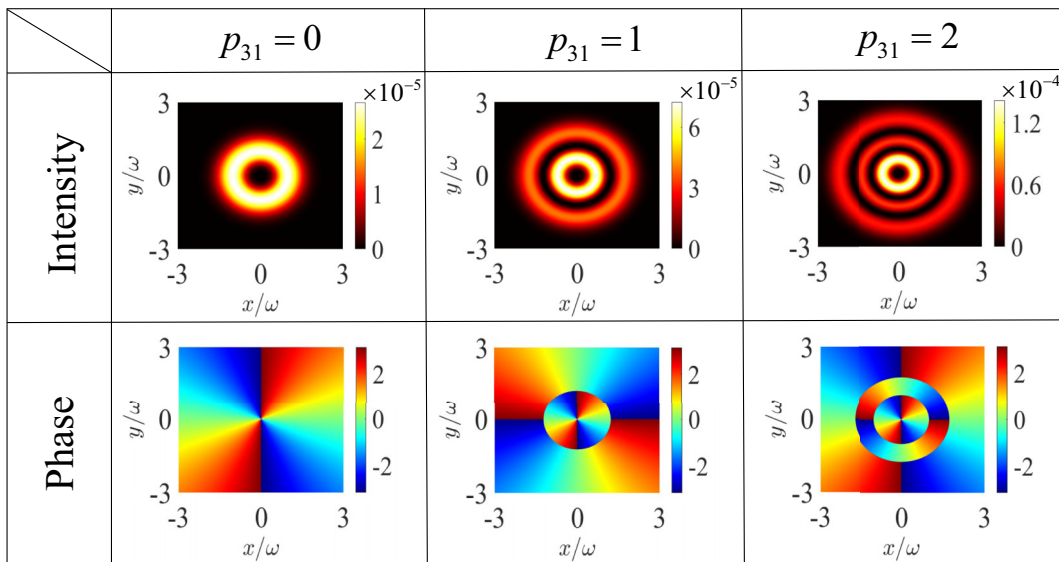

FIG. 4. Intensity and phase patterns of the output vortex signal field at $z = 0$ as a function of (x, y) for different modes of the vortex probe field: $l_{31} = 2$, $p_{31} = 0, 1, 2$. $\Omega_{p0} = 0.01\gamma$, $\alpha = 500$, and the other parameters are same as in Fig. 3.

When the incident probe field is LG_0^2 mode, i.e., $p_{31} = 0$ and $l_{31} = 2$, the intensity distribution of the signal field exhibits a doughnut-shaped pattern, while the helical phase profile displays two periods along the azimuthal direction with the phase of each period is 2π (see the left column in Fig. 4). Besides, a phase singularity occurs at the central dark hole. When the TC remains unchanged and the RI is nonzero, as shown by the middle and right columns in Fig. 4. we can observe multiple bright rings in the intensity pattern of the signal field, where multiple phase zones also appear from the core to the border of the corresponding phase pattern. It is worth noting that the numbers of the bright rings and phase zones are equal to $p_{31} + 1$ and the number of period of helical phase is equal to $|l_{31}|$. That is to say, the OAM information can be completely transferred from the incident vortex probe field to the generated vortex signal field.

Previous studies have demonstrated that the phase mismatch would influence the exchange of optical vortices [41,48]. In the following, we also explore the effect of phase mismatch on the transfer of optical vortices in the backward FWM process. To include the effect of phase mismatch, we should add an additional term into Eq. (14). The geometrical phase-mismatch term can be introduced with the form

$$\Delta k = (\vec{k}_p - \vec{k}_{c2} + \vec{k}_{c1} - \vec{k}_s) \cdot \vec{e}_z. \quad (26)$$

where $\vec{e}_z$ denotes the unit vector along the z axis. $\vec{k}_p, \vec{k}_{c1}, \vec{k}_{c2}$, and $\vec{k}_s$ are the wave vectors of the probe, control, pumping, and signal fields, respectively. It is worth noting that the phase mismatch Δk can be generated by introducing a small angle between the propagation directions of the probe and pump fields. For the nonzero phase mismatch, i.e., $\Delta k \neq 0$, Eq. (16) is modified as

$$-\frac{\partial \Omega_s}{\partial z} - i\Delta k \Omega_s = i\frac{\alpha\gamma}{2L}\rho_{41}. \quad (27)$$

Here, we only consider the optimal condition of $|\Omega_{c1}| = |\Omega_{c2}|$. By substituting Eqs. (11) and (12) into Eqs. (15) and (27) and using the initial conditions of $\Omega_p(z = 0) = \Omega_p(0)$ and $\Omega_s(z = L) = 0$, we obtain

$$\Omega_s(z = 0) = \frac{\alpha}{(\alpha - 2i\Delta kL) + 2\beta \cot\left(\frac{\beta}{2}\right)}\Omega_p(0), \quad (28)$$

with $\beta = [(\Delta kL)^2 + i\alpha\Delta kL]^{1/2}$. Figure 5 shows the curve of the dimensionless intensity $|\Omega_s(0)|^2/|\Omega_p(0)|^2$ of the output signal field at $z = 0$ versus ΔkL. As expected, the existence of phase mismatch would be detrimental to the high-efficiency transfer of optical vortices [41]. Specifically, the conversion efficiency monotonically decreases from 98.4% to 56.6% as ΔkL increases from 0 to 20. In other words, the phase mismatch would suppress the output intensity of the vortex signal field. Meanwhile, the phase-mismatch term ΔkL in Eq. (28) would induce an additional phase shift, which results in the whole helical phase pattern suffering a clockwise rotation without phase distortion (see the inset in Fig. 5).

2. Second case: Both Ω_p and Ω_{c1} are vortex beams

Next, we consider the case that both Ω_p and Ω_{c1} are vortex beams, which can be described by Eq. (22). It can be seen from Eq. (18) that the generated signal field Ω_s is proportional
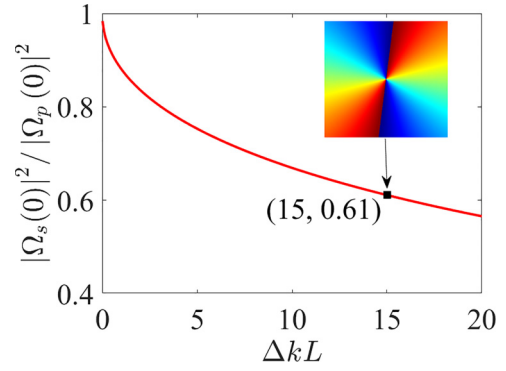

FIG. 5. The dimensionless intensity of the output signal field $|\Omega_s(0)|^2/|\Omega_p(0)|^2$ versus the phase mismatch ΔkL. The inset shows the phase pattern of the output signal field when the phase mismatch is $\Delta kL = 15$ and the probe field is LG_2^0. Other parameters are the same as in Fig. 4(f).

to the product of the weak probe field Ω_p and the strong control field Ω_{c1}.

In Figs. 6 and 7, we plot the intensity and helical phase profiles of the output signal field at $z = 0$ for different OAM combinations of the probe and control fields with $\Omega_{p_0} = 0.01\gamma$ and $\Omega_{c1_0} = \gamma$, respectively. Subsequently, the corresponding linear-superposition LG components of the output signal field are shown in Table I. One can find that the generated signal field develops a new OAM state with auxiliary assist of the vortex control field, which is different from the findings in Fig. 4. When the incident probe field is LG_0^2 ($p_{31} = 0, l_{31} = 2$) mode and the control field is LG_0^1 ($p_{42} = 0, l_{42} = 1$) mode, the product of the two single-ring vortex beams makes the generated signal field become a new single-ring optical vortex. As l_{42} increases from 1 to 5, the increase of the ring radius of the vortex control field leads to the radial extension of the intensity overlap of the probe and control fields, thereby increasing the ring radius of the generated vortex signal field [see the first row in Fig. 6]. Accordingly, the number of period of the helical phase increases from 3 to 7 [see the first row in Fig. 7]. As shown in Table I, the generated signal field comprises only one LG component with the total TC of $l_{31} + l_{42}$. In essence, the generated signal field is still a pure LG mode. For $p_{31} > 0$, the generated signal field shows the complete different intensity and phase distributions. When the probe field is LG_1^2 mode, as shown in the second row of Figs. 6 and 7, it is found that two bright rings and two phase zones appear from the core to the border of the intensity and phase patterns. The maximal intensity of the signal field is shifted from the inner ring to the outer ring and its TC increases from 3 to 7 with increasing l_{42} from 1 to 5. When the probe field is LG_2^2 mode, we can observe a double-ring intensity pattern for $l_{42} = 1$ and a triple-ring pattern for $l_{42} = 3, 5$ (see the third row in Fig. 6). Meanwhile, the helical phase space of the output signal field is divided into three zones along the radial direction (see the third row in Fig. 7). In fact, the single-ring control field carrying OAM acts as a intensity filter and an OAM controller, which can modify the intensity and phase distributions of the output signal field. For $p_{31} > 0$, the generated signal field consists of two or more LG components and each of the componential
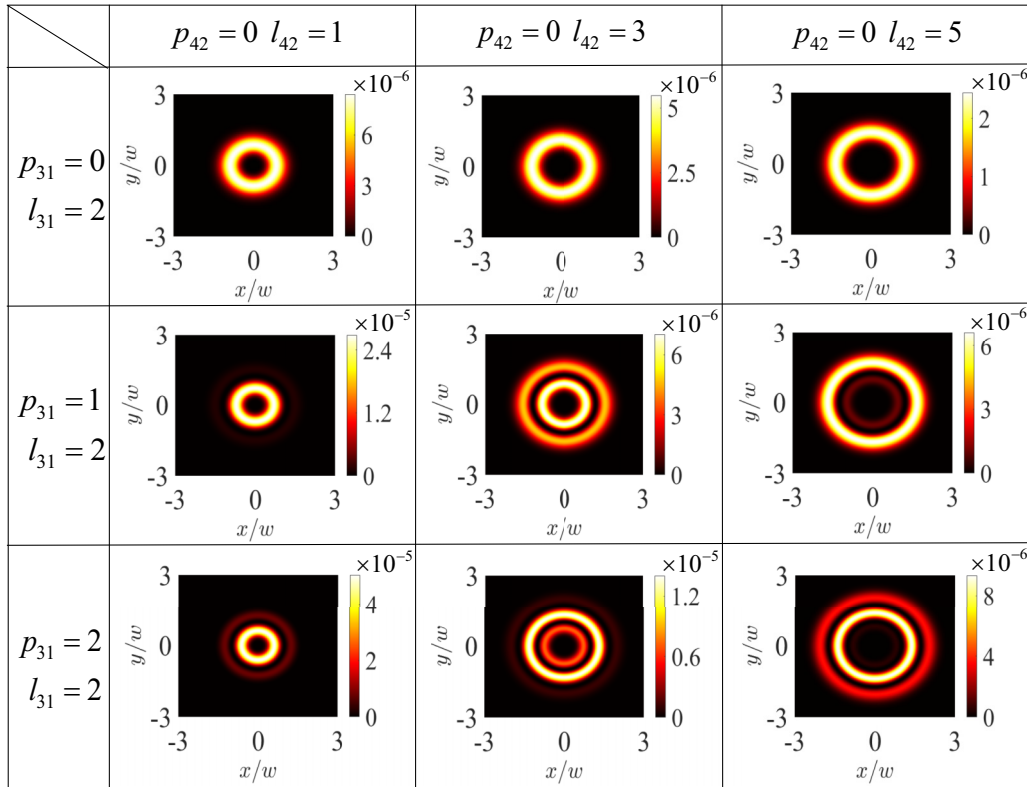
FIG. 6. The intensity patterns of the output vortex signal field at $z = 0$ as a function of (x, y) for different LG modes of the input probe and control fields with $p_{31} \in 0, 1, 2$, $p_{42} = 0$, $l_{31} = 2$, $l_{42} \in 1, 3, 5$, and $\Omega_{c1_0} = \gamma$. Other parameters are the same as in Fig. 4.
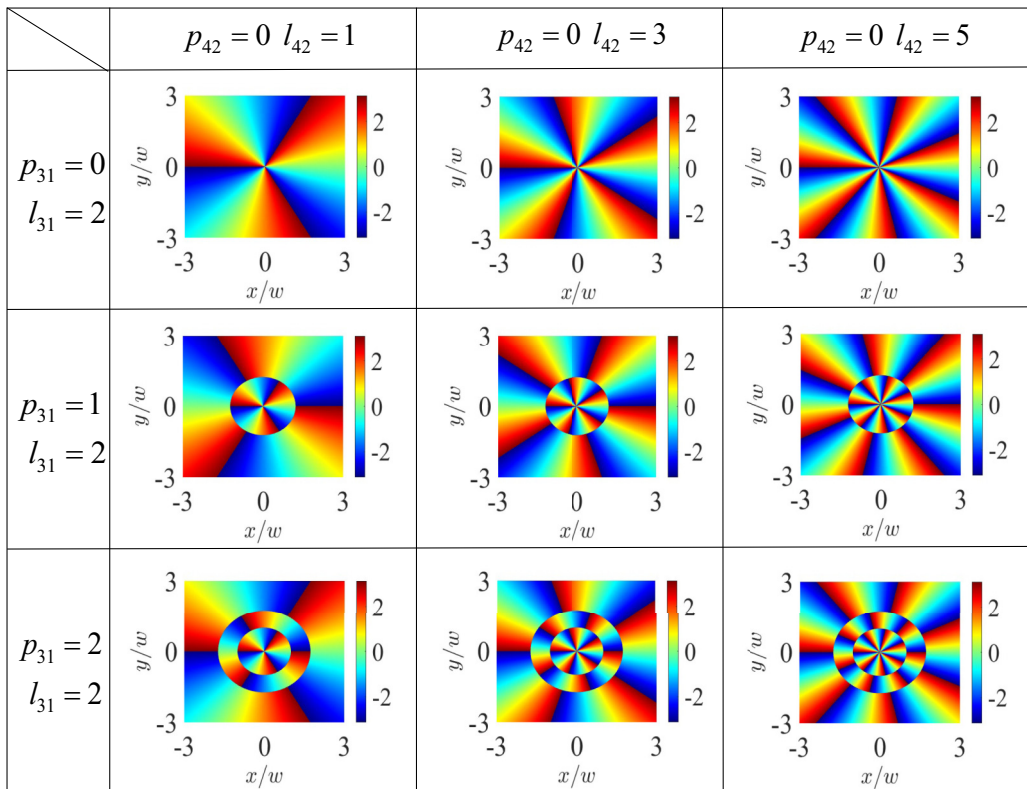

FIG. 7. The corresponding phase patterns of the output signal field $\Omega_s(z = 0)$ as a function of (x, y). The parameters used here are the same as in Fig. 6.

TABLE I. Linear superposition LG components of the output signal field at $z = 0$ for different OAM combinations of the incident probe and control fields.

	$p_{42} = 0, l_{42} = 1$	$p_{42} = 0, l_{42} = 3$	$p_{42} = 0, l_{42} = 5$
$p_{31} = 0, l_{31} = 2$	$\sqrt{3}\mathrm{LG}_0^3$	$2\sqrt{5}\mathrm{LG}_0^5$	$6\sqrt{14}\mathrm{LG}_0^7$
$p_{31} = 1, l_{31} = 2$	$\sqrt{3}(\mathrm{LG}_1^3 - \mathrm{LG}_0^3)$	$2\sqrt{5}(\mathrm{LG}_1^5 - 3\mathrm{LG}_0^5)$	$6\sqrt{14}(\mathrm{LG}_1^7 - 5\mathrm{LG}_0^7)$
$p_{31} = 2, l_{31} = 2$	$\sqrt{3}(\mathrm{LG}_2^3 - \mathrm{LG}_1^3)$	$2\sqrt{5}(\mathrm{LG}_2^5 - 3\mathrm{LG}_1^5 + 3\mathrm{LG}_0^5)$	$6\sqrt{14}(\mathrm{LG}_2^7 - 5\mathrm{LG}_1^7 + 10\mathrm{LG}_0^7)$

mode has the TC of $l_{31} + l_{42}$ due to OAM conservation in the FWM process (see Table I). Thus, the generated signal field becomes a mixing LG mode, which is completely different from the case of $p_{31} = 0$.

We note that, very recently, some theoretical schemes for the coherent transfer of optical vortices in atomic media have been proposed [44,45,51,52,54,57]. Comparing with these schemes, the major differences in our proposal are the following: First, the conversion efficiency of optical vortices can approach nearly 100% via backward FWM in a dense atomic medium with large OD, which is greatly improved compared with previous schemes [44,51,52,54,57]. Second, the complete energy transfer of optical vortices originates from the perfect competition between linear absorption and parametric gain in backward FWM, which avoids the rather complicated spatial modulation for two strong applied fields in Ref. [45]. Third, under the double action of the probe and control fields carrying OAM, the generated signal field develops a new OAM state, which has not been explored in Ref. [45].

Such a transfer of optical vortices may find application in the creation of structured light by another light [63] and in the conversion of phase information from a given input frequency to a completely different frequency. Extending our approach into the solid-state system, one could create a vortex at a wavelength which is not possible to do directly with standard optics (e.g., far infrared or ultraviolet) [64]. In addition, the transfer of optical vortices is a possible tool for the manipulation of information encoded into OAM of light and has implications on the inscription and storage of phase information in light-matter coupling schemes [37].

B. Composite vortices

In this section, we investigate the characteristics of the composite vortices where both the vortex probe field $\Omega_p(0) = \Omega_p(r, \phi)$ and the vortex signal field $\Omega_s(L) = \Omega_s(r, \phi)$ are incident on the atomic medium. Solving Eqs. (13) and (14) with new boundary conditions, the analytical expressions of the output signal field at $z = 0$ can be written as

$$\Omega_s(z = 0) = A\Omega_p(0) + B\Omega_s(L), \quad (29)$$

with $A = (e^s - 1)\Omega_{c2}^*\Omega_{c1}/(|\Omega_{c2}|^2 e^s - |\Omega_{c1}|^2)$, $B = (|\Omega_{c2}|^2 - |\Omega_{c1}|^2)/(|\Omega_{c2}|^2 e^s - |\Omega_{c1}|^2)$ for $|\Omega_{c1}| \neq |\Omega_{c2}|$ and $A = \alpha/(\alpha + 4)$, $B = 4/(\alpha + 4)$ for $|\Omega_{c1}| = |\Omega_{c2}|$. A and B represent the weights of the incident probe and signal fields, respectively. Figure 8 shows the values of A and B versus the control field Ω_{c1}. It can be seen from Fig. 8 that the weights of the input vortex probe and signal fields can be controlled via adjusting the control field Ω_{c1}.

According to Eq. (29), a backward composite vortex beam can be generated by the collinear superposition of two

incident vortex beams. The intensity and phase profiles of the output signal field $\Omega_s(z = 0)$ are displayed in Figs. 9 and 10, respectively, for $\Omega_{c1} = 0.4\gamma$, 1.6γ, and 2.8γ. Different combinations of the LG modes for the incident probe and signal fields are considered, i.e., $(l_{31}, l_{41}) = (2, 3)$, $(2, 4)$, and $(2, 5)$ with $p_{31} = p_{41} = 0$. The intensity of the incident signal field is chosen as $\Omega_{s0} = 0.01\gamma$ and the other parameters are the same as in Fig. 4. Obviously, the intensity and phase patterns of the composite vortex field are sensitive to the control field Ω_{c1}. In the case of $\Omega_{c1} = 0.4\gamma$, the weight of the input signal field is approximately equal to 0 and the input probe field dominates. Consequently, the intensity and phase patterns of the output signal field at $z = 0$ are similar to those of the input probe field $\Omega_p(0)$ (see the left columns of Figs. 9 and 10). As Ω_{c1} increases to 1.6γ, the weights of the input probe and signal fields are equal, i.e., $A = B$. In this situation, the complete interference between the two LG modes produces annularly distributed intensity vanishes (dark spots) in the overlapped region and the number of dark spots along the ring zone is calculated by $N = |l_{41} - l_{31}|$ (see the middle column of Fig. 9). Accordingly, the same number of phase singularities occur at the positions of dark spots (see the middle column of Fig. 10). When $\Omega_{c1} = 2.8\gamma$, $A < B$, the input vortex signal field dominates in the interference of two optical vortices. It is found that these local dark spots would collapse to a big dark spots and the positions of phase singularities are closer to the central point (see the right column of Figs. 9 and 10). Therefore, we can effectively manipulate the composite vortex beam via adjusting the control field Ω_{c1}.

Finally, we give the possible experimental realization of the proposed vortex backward FWM. According to Refs. [37,38,62], the diode laser provides the laser source of 795 nm. The generated laser is split into the experimental
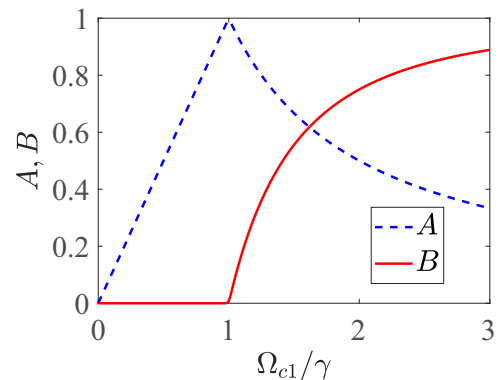

FIG. 8. The weights A, B of the incident probe and signal fields as a function of the control field Ω_{c1}. Other parameters are the same as in Fig. 4.
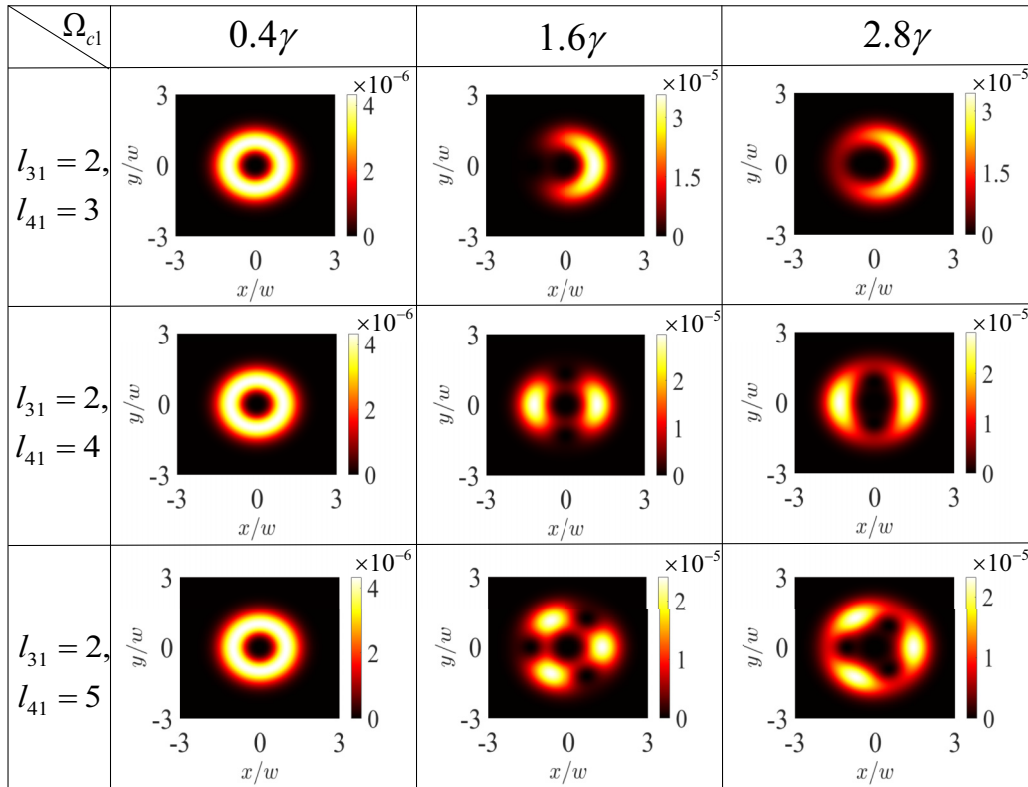
FIG. 9. The intensity patterns of the output signal field $\Omega_s(z = 0)$ as a function of x and y for different LG modes of the input probe and signal fields, i.e., $(l_{31}, l_{41}) = (2, 3)$, $(2,4)$, and $(2,5)$ and for different control fields $\Omega_{c1} = 0.4\gamma$, 1.6γ, and 2.8γ. $\Omega_{s0} = 0.01\gamma$ and the other parameters are the same as in Fig. 4.
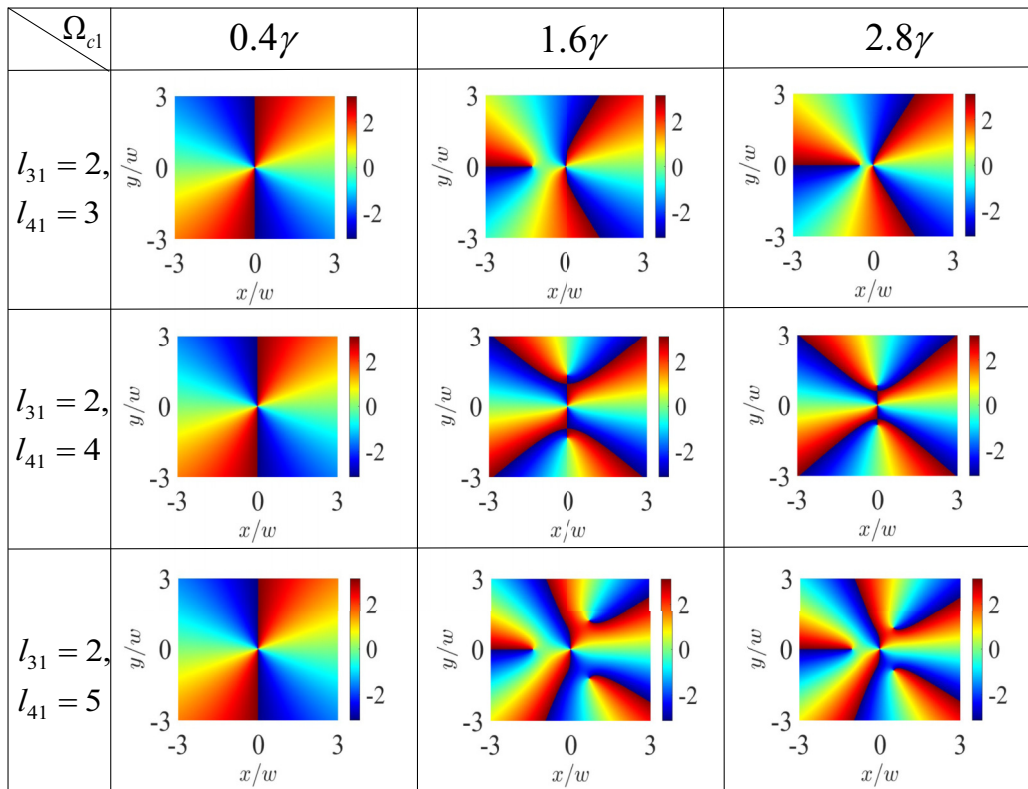

FIG. 10. The corresponding phase patterns of the output signal field $\Omega_s(z = 0)$ as a function of x and y. The parameters used here are the same as in Fig. 8.

beams by beam splitters. Each beam passes an acousto-optic modulator to modulate the intensity, frequency and pulse sequence. The frequencies of the laser beams are modulated to satisfy the resonant light-atom interaction of Fig. 1(a). The weak probe beam and the strong control beam propagate through the atomic ensemble in the forward $(+z)$ direction, while the weak signal beam and the strong pump beam propagates in the opposite direction. In part A, the forward probe beam Ω_p (or both the probe beam Ω_p and the control beam Ω_{c1}) can be transformed into light beams carrying OAM using computer-controlled spatial light modulators (SLMs). Then the new vortex signal beam is generated through the vortex backward FWM. In part B, both the forward probe beam Ω_p and the backward signal beam Ω_s are transformed into vortex beams using computer-controlled SLM. Subsequently, a composite vortex beam described by the output signal field is generated through the resonant light-atom interaction. In the above cases, one part of the generated signal beam passing through the atomic ensemble is detected by photodiodes, and the other part is monitored by a CCD camera to analyze the transverse spatial structure.

IV. CONCLUSION

In conclusion, we have theoretically investigated the transfer and manipulation of optical vortices in a cold atomic ensemble with four-level double-Λ configuration. The OAM transfer between different frequencies would take place via the backward FWM process. It is demonstrated that the matched control and pump intensities are the optimal condition for achieving the nearly 100% vortex conversion efficiency in a dense atomic ensemble with a large OD. We have given a suitable physical interpretation for the complete energy transfer of optical vortices via the perfect competition between linear absorption and parametric gain in the backward FWM. It has also been found that the effect of phase mismatch would reduce the conversion efficiency of optical vortices. Furthermore, it is found the generated signal field would develop a new OAM state with auxiliary assist of the vortex control field. The pure or mixing LG mode can be effectively switched via different OAM combinations of the probe and control fields. Finally, the vortex probe and signal fields initially acting on the cold atomic ensemble generates a composite vortex for the output signal field. It is seen that the OAM state of the composite vortex beam can be controlled via adjusting the intensity of the control field. Our scheme may have potential applications in OAM-based optical communication and optical information process.

[1] D. G. Grier, Nature (London) **424**, 810 (2003).

[2] J. Wang, J. Y. Yang, I. M. Fazal, N. Ahmed, Y. Yan, H. Huang, Y. Ren, Y. Yue, S. Dolinar, M. Tur, and A. E. Willner, Nat. Photonics **6**, 488 (2012).

[3] N. Bozinovic, Y. Yue, Y. Ren, M. Tur, P. Kristensen, H. Huang, A. E. Willner, and S. Ramachandran, Science **340**, 1545 (2013).

[4] M. Padgett and R. Bowman, Nat. Photonics **5**, 343 (2011).

[5] *The Angular Momentum of Light*, edited by D. L. Andrews and M. Babiker (Cambridge University Press, Cambridge, 2012).

[6] L. Allen, M. J. Padgett, and M. Babiker, Prog. Opt. **39**, 291 (1999).

[7] F. Gori, G. Guattari, and C. Padovani, Opt. Commun. **64**, 491 (1987).

[8] A. Ostrovsky, C. Rickenstorff-Parrao, and V. Arrizón, Opt. Lett. **38**, 534 (2013)

[9] L. Allen, M. W. Beijersbergen, R. J. C. Spreeuw, and J. P. Woerdman, Phys. Rev. A **45**, 8185 (1992).

[10] P. Vaity and L. Rusch, Opt. Lett. **40**, 597 (2015).

[11] K. Dai, J. Miller, W. Li, R. Watkins, and E. Johnson, Opt. Lett. **46**, 3332 (2021).

[12] J. Leach, J. Courtial, K. Skeldon, S. M. Barnett, S. Franke-Arnold, and M. J. Padgett, Phys. Rev. Lett. **92**, 013601 (2004).

[13] G. C. G. Berkhout and M. W. Beijersbergen, Phys. Rev. Lett. **101**, 100801 (2008).

[14] J. M. Hickmann, E. J. S. Fonseca, W. C. Soares, and S. Chávez-Cerda, Phys. Rev. Lett. **105**, 053904 (2010).

[15] E. Brasselet, Phys. Rev. Lett. **121**, 033901 (2018).

[16] S. Chen, Y. Cai, G. Li, S. Zhang, and K. W. Cheah, Laser Photonics Rev. **10**, 322 (2016).

[17] Y. Zhang, J. Gao, and X. Yang, Adv. Opt. Mater. **7**, 1801486 (2019).

[18] P. Chen, S. J. Ge, L. L. Ma, W. Hu, V. Chigrinov, and Y. Q. Lu, Phys. Rev. Appl. **5**, 044009 (2016).

[19] S. E. Harris, Phys. Today **50**, 36 (1997).

[20] S. Qamar, S. Y. Zhu, and M. S. Zubairy, Phys. Rev. A **61**, 063806 (2000).

[21] R. G. Wan and T. Y. Zhang, Opt. Express **19**, 25823 (2011).

[22] F. Zhou, Y. Qi, H. Sun, D. Chen, J. Yang, Y. Niu *et al.*, Opt. Express **21**, 12249 (2013).

[23] G. L. Cheng and A. X. Chen, Opt. Express **25**, 4483 (2017).

[24] J. H. Wu, S. A. R. Horsley, M. Artoni, and G. C. La Rocca, Light: Sci. Appl. **2**, e54 (2013).

[25] H. Yang, T. Zhang, Y. Zhang, and J. H. Wu, Phys. Rev. A **101**, 053856 (2020).

[26] C. Hang, G. Huang, and V. V. Konotop, Phys. Rev. Lett. **110**, 083604 (2013).

[27] Z. Zhang, Y. Zhang, J. Sheng, L. Yang, M. A. Miri, D. N. Christodoulides, B. He, Y. Zhang, and M. Xiao, Phys. Rev. Lett. **117**, 123601 (2016).

[28] V. E. Lembessis and M. Babiker, Phys. Rev. A **82**, 051402(R) (2010).

[29] N. Radwell, T. W. Clark, B. Piccirillo, S. M. Barnett, and S. Franke-Arnold, Phys. Rev. Lett. **114**, 123603 (2015).

[30] H. R. Hamedi, V. Kudriašov, J. Ruseckas, and G. Juzeliūnas, Opt. Express **26**, 28249 (2018).

[31] X. Dai, X. Hao, R. Jin, C. Peng, and C. Ding, J. Appl. Phys. **129**, 224303 (2021).

[32] J. Che, P. Zhao, D. Ma, and Y. Zhang, Opt. Express **28**, 18343 (2020).

[33] N. Jia, J. Qian, T. Kirova, G. Juzeliūnas, and H. R. Hamedi, Opt. Express **28**, 36936 (2020).

[34] D. Moretti, D. Felinto, and J. W. R. Tabosa, Phys. Rev. A **79**, 023825 (2009).

[35] L. Veissier, A. Nicolas, L. Giner, D. Maxein, A. S. Sheremet, E. Giacobino, and J. Laurat, Opt. Lett. **38**, 712 (2013).

[36] S. Barreiro, J. W. R. Tabosa, J. P. Torres, Y. Deyanova, and L. Torner, Opt. Lett. **29**, 1515 (2004).

[37] G. Walker, A. S. Arnold, and S. Franke-Arnold, Phys. Rev. Lett. **108**, 243601 (2012).

[38] D. S. Ding, Z. Y. Zhou, B. S. Shi, X. B. Zou, and G. C. Guo, Opt. Lett. **37**, 3270 (2012).

[39] C. Yu and Z. Wang, Phys. Rev. A **103**, 013518 (2021).

[40] J. Qiu, Z. Wang, D. Ding, Z. Huang, and B. Yu, Phys. Rev. A **102**, 033516 (2020).

[41] H. R. Hamedi, J. Ruseckas, and G. Juzeliūnas, Phys. Rev. A **98**, 013840 (2018).

[42] Y. Hong, Z. Wang, D. Ding, and B. Yu, Opt. Express **27**, 29863 (2019).

[43] O. N. Verma, R. K. Pandey, R. R. Yadav, and A. Patel, Phys. Rev. A **106**, 053713 (2022).

[44] S. H. Asadpour, E. Paspalakis, and H. R. Hamedi, Phys. Rev. A **103**, 063705 (2021).

[45] H. R. Hamedi, E. Paspalakis, G. Žlabys, G. Juzeliūnas, and J. Ruseckas, Phys. Rev. A **100**, 023811 (2019).

[46] J. Ruseckas, V. Kudriašov, I. A. Yu, and G. Juzeliūnas, Phys. Rev. A **87**, 053840 (2013).

[47] H. R. Hamedi, J. Ruseckas, E. Paspalakis, and G. Juzeliūnas, Phys. Rev. A **99**, 033812 (2019).

[48] S. H. Asadpour, Ziauddin, M. Abbas, and H. R. Hamedi, Phys. Rev. A **105**, 033709 (2022).

[49] D. S. Ding, W. Zhang, Z. Y. Zhou, S. Shi, G. Y. Xiang, X. S. Wang, Y. K. Jiang, B. S. Shi, and G. C. Guo, Phys. Rev. Lett. **114**, 050502 (2015).

[50] M. T. Cao, Y. Yu, L. Y. Zhang, F. J. Ye, Y. L. Wang, D. Wei, P. Zhang, W. G. Guo, S. G. Zhang, H. Gao, and F. L. Li, Opt. Express **22**, 20177 (2014).

[51] J. Qiu, Z. P. Wang, D. S. Ding, W. B. Li, and B. L. Yu, Opt. Express **28**, 2975 (2020).

[52] Z. Wang, Y. Zhang, E. Paspalakis, and B. Yu, Phys. Rev. A **102**, 063509 (2020).

[53] X. Deng, T. Shui, and W. X. Yang, Front. Phys. **10**, 877859 (2022).

[54] M. Mahdavi, Z. Amini Sabegh, M. Mohammadi, M. Mahmoudi, and H. R. Hamedi, Phys. Rev. A **101**, 063811 (2020).

[55] Rahmatullah, M. Abbas, Ziauddin, and S. Qamar, Phys. Rev. A **101**, 023821 (2020).

[56] L. Wang, X. Zhang, A. Li, Z. Kang, H. Wang, and J. Gao, J. Lumin. **228**, 117628 (2020).

[57] M. Mahdavi, Z. A. Sabegh, H. R. Hamedi, and M. Mahmoudi, Phys. Rev. B **104**, 094432 (2021).

[58] C. Ding, J. Li, X. Dai, R. B. Jin, and X. Hao, Opt. Express **29**, 36840 (2021).

[59] D. A. Steck, Rubidium 87 D line data, available online at http://steck.us/alkalidata

[60] Y. F. Hsiao, H. S. Chen, P. J. Tsai, and Y. C. Chen, Phys. Rev. A **90**, 055401 (2014).

[61] H. Kang, G. Hernandez, J. Zhang, and Y. Zhu, J. Opt. Soc. Am. B **23**, 718 (2006).

[62] Z. Y. Liu, J. T. Xiao, J. K. Lin, J. J. Wu, J. Y. Juo, C. Y. Cheng, and Y. F. Chen, Sci. Rep. **7**, 15796 (2017).

[63] Z. Dutton and J. Ruostekoski, Phys. Rev. Lett. **93**, 193602 (2004).

[64] N. A. Chaitanya, S. C. Kumar, K. Devi, G. K. Samanta, and M. Ebrahim-Zadeh, Opt. Lett. **41**, 2715 (2016).